Exploiting close zonal-sampling of HIRDLS profiles near turnaround latitude to investigate missing drag in chemistry-climate models near 60°S

Laura A. Holt[1,*], Colby M. Brabec[2,*], and M. Joan Alexander[1]

[1]NorthWest Research Associates, Boulder, Colorado
[2]Department of Atmospheric and Oceanic Science, University of Colorado, Boulder, Colorado
[*]The authors contributed equally to this work

Key Points:

- GW momentum fluxes near 60°S are much larger locally over orography, but contribution to zonal mean is larger over nonorographic regions
- GW momentum flux in winter upper stratosphere is highly correlated with near surface winds over orographic regions
- HIRDLS zonal drag estimates suggest CCMI-1 models have insufficient zonal drag and majority of missing drag is over nonorographic regions

Corresponding author: Laura Holt, laura@nwra.com

Abstract

This study exploits the high-density zonal sampling at the turnaround latitude of the High Resolution Dynamics Limb Sounder (HIRDLS) in the Southern Hemisphere to investigate the missing drag in chemistry-climate models near 60°S. Gravity wave (GW) properties including amplitude, zonal wavenumber, vertical wavelength, and momentum flux are estimated with a wavelet analysis method based on the S-transform. Monthly means of GW properties compare well with estimates from previous studies. We further investigate the contribution to GW momentum flux above orographic and nonorographic regions and find that while fluxes are much larger locally over orographic regions, the contribution to the zonal mean is roughly 3 times smaller than the contribution over nonorographic regions. We also investigate the relationship with the zonal wind and find that GW momentum flux is highly correlated with the near surface winds over orographic regions. In addition to momentum flux, we also provide estimates of the zonal drag and use these estimates to evaluate the current GW parameterizations and resolved wave forcing in models participating in phase 1 of the Chemistry-Climate Model Initiative (CCMI-1). The HIRDLS zonal drag estimates suggest that the CCMI-1 models have insufficient zonal drag, especially in June, July, and August, and that the majority of the missing drag is over nonorographic regions. Our discussion includes implications for the Brewer-Dobson Circulation and ozone hole.

1 Introduction

Gravity waves (GWs) play a key role in the dynamics of the atmosphere, but it remains a challenge to represent them in chemistry-climate models (CCMs). This contributes to biases in temperatures and winds in the Southern Hemisphere stratosphere. Generally, winds are too strong and temperatures too cold compared to observations. Additionally, the stratospheric final warming in the Southern Hemisphere is typically one or two weeks late in CCMs compared to observations (Eyring et al., 2010; Butchart et al., 2011). Although the reasons for these biases are not completely understood, it is generally thought that missing Southern Hemisphere wave drag in models is a major culprit.

Possible sources of the missing wave drag include inadequate continental orographic GW drag (McLandress et al., 2012), orographic GW drag from small, unresolved islands (Alexander et al., 2009; Alexander & Grimsdell, 2013), lateral propagation of GWs generated at other latitudes (e.g., Sato et al., 2009; Yamashita et al., 2010; Sato et al., 2012; Jiang et al., 2013; Krisch et al., 2017; Thurairajah et al., 2017; Strube et al., 2021), and nonorographic GWs generated by fronts and convection (Hendricks et al., 2014; Shibuya et al., 2015; Holt et al., 2017). Several observational and modeling studies have documented large, intermittent momentum fluxes over the Southern Ocean (e.g., Hertzog et al., 2008, 2012; Plougonven et al., 2013; Jewtoukoff et al., 2015), supporting the case for large-amplitude nonorographic GWs generated by strong convection. Studies have also shown improved model biases and improved timing of the stratospheric final warming in the Southern Hemisphere when the gravity wave parameterization is based on an intermittent source function (de la Cámara & Lott, 2015; de la Cámara et al., 2016). Understanding the sources of the missing drag and correcting the deficiencies in modeled GW effects is a high priority since the resulting model biases in wind and temperature hinder our ability to realistically model the ozone hole and its recovery, which also has implications for our ability to model surface climate change (e.g., Arblaster et al., 2014).

McLandress et al. (2012) showed that adding extra orographic GW drag at 60°S in a CCM resulted in a significant improvement in the cold-pole bias and timing of the vortex breakdown, which in turn affect the ozone hole depth. Garcia et al.

(2017) achieved similar improvements in the cold-pole bias in a CCM by increasing the parameterized orographic GW drag in the Southern Hemisphere. These approaches are justified as long as the observational guidance remains ambiguous for constraining the missing Southern Hemisphere drag, but these methods are not ideal. For example, while strong localized orographic GW drag may have similar effects on the zonal mean as more zonally uniform drag, there can be dramatically different interactions with Rossby waves and horizontal and vertical mixing effects on tracers. Ideally we would get the stratospheric wind and temperature responses to GW drag correct and for the right reasons, and for this it is essential that the tunable parameters in CCMs be constrained by observations.

In this paper, we exploit the close zonal sampling of the High Resolution Dynamics Limb Sounder (HIRDLS) at the turnaround latitude to obtain estimates of the missing drag in the Southern Hemisphere. At the turnaround latitude (∼63.4°S), HIRDLS provides a wealth of information on waves spanning zonal wavenumbers 1 through 90. This information has not yet been utilized to investigate missing Southern Hemisphere drag. While previous studies have used HIRDLS to look at the largest scale waves between wavenumbers 1 through 8 in the tropics (Alexander et al., 2010) or global properties of small-scale GWs (Alexander et al., 2008; Ern et al., 2011; Wright et al., 2010), none have focused on the turnaround latitude in the Southern Hemisphere.

Waves of all scales, from planetary waves to small-scale GWs, contribute to the drag on the zonal wind and the driving of the Brewer-Dobson circulation near 60°S. GWs with higher zonal wavenumbers are only observable with HIRDLS where zonal sampling occurs more frequently. For example, zonal measurements near the equator are ∼400 km apart which means the shortest observable wavelength is ∼800 km, whereas the zonal sampling near the turnaround latitude is between ∼70-140 km. This makes sampling at the high latitudes ideal for investigating the missing drag near 60°S.

This paper is organized as follows: in Section 2 we describe the data and S-tranform method we use to estimate GW properties. In Section 3 we describe the observed wave properties, including momentum flux and wave statistics. Finally, in Section 4 we present estimates of potential drag and compare HIRDLS GW potential drag to parameterized and resolved drag in CCMs and discuss the implications for the Brewer-Dobson Circulation and ozone hole.

2 Data and Methodology

2.1 HIRDLS Temperature Profiles

The HIRDLS instrument on board NASA's Aura satellite is a limb-scanning infrared radiometer. Aura is in a sun-synchronous, polar orbit with an orbital period of 99 minutes making approximately 14.9 revolutions per day (Gille et al., 2008). The basis of our analysis uses HIRDLS high vertical resolution temperature profiles with ∼1 km vertical resolution and ∼70-140 km horizontal resolution. This study uses version 7 of the Level 2 HIRDLS data for the period from January 2005 to March 2008, with a focus on May through November (days 121 to 334) in the Southern Hemisphere winter and spring seasons. Note that each year a few days have incomplete measurements, so days listed in Table 1 were removed. Occasionally, profiles were flagged as bad data, showing single-level spikes in the temperature profile as large as 10 times the normal temperature perturbation. Further investigation found that temperature quality and cloud top pressure did not flag these cases, so such profiles were removed from the analysis.

Table 1. HIRDLS Data Removed

Year	Days
2005	132, 193, 194, 195, 205, 306, 349, 350
2006	143, 186, 191, 236, 307
2007	163, 194, 310

Figure 1 shows the geographic location of each profile scan for 7 September 2006. HIRDLS provides approximatley 5,530 profile measurements per day and scans vertically at a fixed azimuth of -47° on the anti-sun side of the orbit track. High density zonal sampling occurs near a satellite's turnaround latitude, where the measurement track switches between descending and ascending nodes. For HIRDLS, this turnaround latitude in the Southern Hemisphere is at ∼63.4°S. In this study, we focus on the profiles between 61 and ∼63.4°S that are highlighted pink in Figure 1. For these latitudes, the zonal distance between profiles is ∼20 times larger than the meridional distance between profiles on average. Therefore, the sampling at these latitudes can be assumed to be zonal and we will assume that our analysis provides the zonal component of the horizontal wavenumber and an estimate of the zonal component of the GW momentum flux. Focusing on measurements at these latitudes reduces the number of profiles to roughly 375 per day.

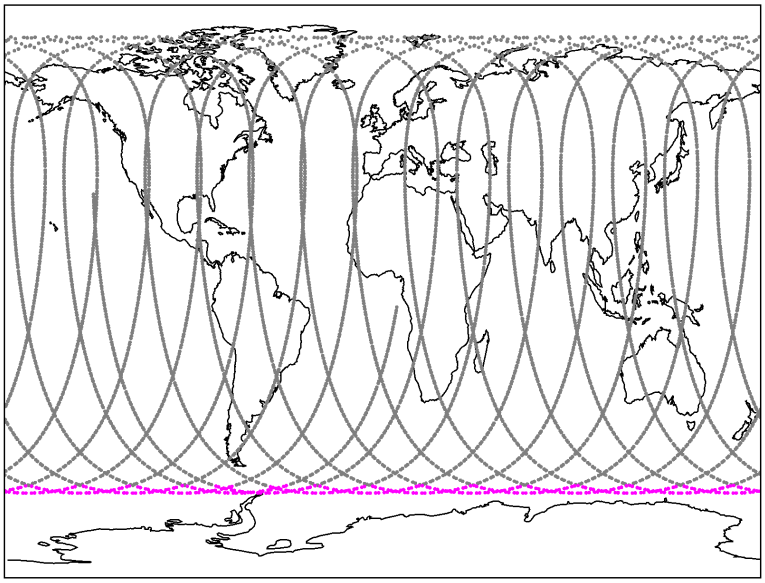

Figure 1. HIRDLS temperature profiles for 7 September 2006. The profiles used in our analysis are highlighted in pink.

2.2 MERRA-2

Winds influence vertically propagating GWs at every stage of the GW lifecycle, from generation to refraction, filtering, and dissipation. We use the MERRA-2 3-hourly, instantaneous, pressure-level assimilated meteorological fields (`doi:10.5067/QBZ6MG944HW0`). This V5.12.4 data has a spatial resolution of 0.5° x 0.625° and 42 vertical levels. Zonal winds between 60 and 66°S are used to investigate the relationship between winds and momentum flux and drag from HIRDLS data.

2.3 CCMI-1

To highlight how our results could be applied to improve chemistry-climate simulations, we use output from the Chemistry-Climate Model Initiative (CCMI-1) (Eyring et al., 2013; Hegglin et al., 2015). We include CCMI-1 models that provide zonal acceleration due to paramaterized orographic and nonorographic GWs and EP flux divergence in the refC1 zonal mean files. This allows us to compare the total wave-driven zonal forcing in the CCMI-1 models to the zonal GW forcing inferred from the HIRDLS analysis in Section 4.1.

2.4 S-Transform Wavelet Analysis

We compute wave properties from the HIRDLS data by using the S-transform (Stockwell et al., 1996) with the method described by Alexander et al. (2008). This analysis provides amplitude, horizontal and vertical wavelength, and momentum flux for GWs observed in HIRDLS temperature profiles. The S-transform is well-suited for analyzing GWs in satellite data and has been used in many other studies with a variety of geophysical datasets (e.g., Stockwell et al., 2007; Alexander & Barnett, 2007; Wright et al., 2010; Wright & Gille, 2013; Hindley et al., 2015, 2016, 2019).

Here we briefly outline the method in Alexander et al. (2008). For each day of HIRDLS measurements, we compute the zonal mean temperature as a function of latitude (in 2.4° bins) and altitude. Then we compute planetary-scale perturbations from the remaining temperature variations using the S-transform. Wave numbers 0-5 are used to define the "large-scale temperature", and we subtract the large-scale temperature from the HIRDLS temperatures to obtain "perturbation" profiles. Next the S-transform is computed for each HIRDLS perturbation profile south of 61°S, providing a complex-valued function of altitude, z and vertical wavelength, λ_z: $\widetilde{T}(z, \lambda_z)$. Then the cospectrum

$$C_{(i,i+1)} = \widetilde{T}_i \widetilde{T}^*_{i+1} = \hat{T}_i \hat{T}_{i+1} e^{i\Delta\phi_{i,i+1}} \tag{1}$$

and the covariance spectrum, $|C_{(i,i+1)}|$, are computed for each adjacent profile pair, i and $i+1$, where the asterisk represents the complex conjugate. For the S-transform analysis, we zero pad the HIRDLS profiles below 10 km and above 70 km to reduce wraparound effects. The covarying temperature amplitude is

$$\hat{T}_{(i,i+1)} = \sqrt{|C_{i,i+1}|}. \tag{2}$$

and the phase difference between profiles is

$$\Delta\phi_{i,i+1} = \tan^{-1} \frac{\Im(C_{i,i+1})}{\Re(C_{i,i+1})} \tag{3}$$

From the horizontal (zonal) phase difference $\Delta\phi_{i,i+1}$, we estimate the zonal wavenumber via

$$k = \frac{\Delta\phi_{i,i+1}}{\Delta r_{i,i+1}} \tag{4}$$

where $\Delta r_{i,i+1}$ is the distance between the adjacent profiles.

Figure 2a highlights a swath of HIRDLS profiles near the turnaround latitude near the Antarctic Peninsula on 7 September 2006. Figure 2b shows temperature perturbation profiles for all of the solid black circles in (a). These temperature perturbations show the wave like structure with height. The tilting of the wave from east to west with altitude above the tip of the Antarctic Peninsula indicates that the wave is propagating westward. Figure 2c shows the covarying temperature amplitude, $\hat{T}$ (Equation 2) as a function of vertical wavelength and altitude for the profile pair highlighted in pink near 60°W. The S-transform reveals that the dominant vertical wavelength is ∼20 km and increases slightly with altitude. The peak amplitude of this wave contribution is ∼15 K near 50 km in altitude. At 50 km there is another peak in the covariance spectrum near 10 km vertical wavelength. These features can also be satisfactorily confirmed by eye in (b). The black lines in (c) indicate the cone of influence for zero-padding effects from the S-transform: the values below and above the black lines are possibly contaminated by these effects and should be used with caution. We choose a vertical wavelength cutoff of 40 km to compromise between including longer wavelength waves and excluding signals that would be largely contaminated by zero-padding effects.

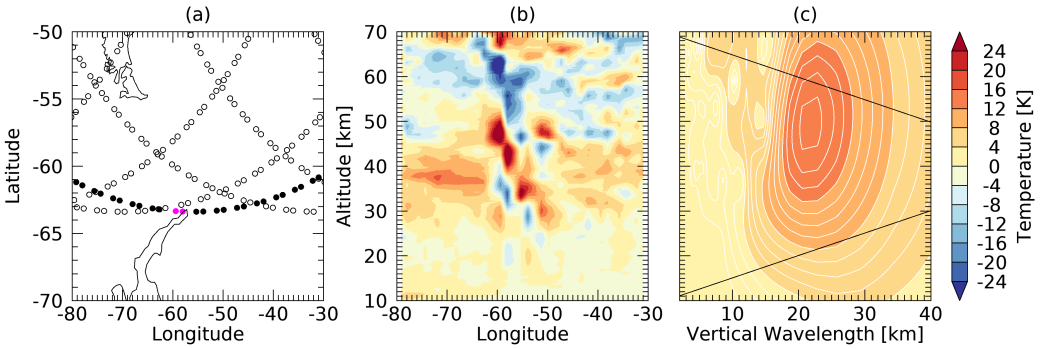

Figure 2. (a) HIRDLS profile locations near the Antarctic Peninsula for 7 September 2006. Solid black circles highlight one swath of HIRDLS profiles south of 61°S, and the solid pink circles highlight one profile pair. (b) Temperature perturbation profiles for the solid black measurement swath in (a). (c) Covarying temperature amplitude, $\hat{T}$ (square root of the covariance spectrum as in Equation 2) as a function of vertical wavelength and altitude for the two profiles in pink in (a). The color bar applies to both (b) and (c), and the white contours in (c) are 1 K. Black lines indicate cone of influence for zero-padding effects from the S-transform.

To estimate the zonal momentum flux for each peak in the covariance spectrum, we use

$$M_{i,i+1}(z,\lambda_z) = \frac{\rho}{2}\lambda_z \frac{k}{2\pi}\left(\frac{g}{N}\right)^2 \left(\frac{\hat{T}_{i,i+1}(z,\lambda_z)}{\bar{T}}\right)^2 \tag{5}$$

where $M_{i,i+1}$ is momentum flux, ρ is density, g is the gravitational acceleration of Earth, N is buoyancy frequency, and $\bar{T}$ is the background temperature. In previous work only one or two peaks in the covariance spectrum were used to compute the momentum flux, and vertical wavelengths were limited to those less than 25 km (Alexander et al., 2008; Wright et al., 2010). Here we use all of the peaks in the covariance spectrum with vertical wavelengths less than 40 km since the strength of winds in the Southern Hemisphere near the turnaround latitude can be particularly strong, and therefore we expect HIRDLS to detect waves with longer vertical wavelengths. We further stipulate that the peaks must be higher than the HIRDLS noise threshold of 0.5 K. We identify all the peaks in $C_{i,i+1}$ at each altitude and then use a quadratic

fit to estimate the true temperature amplitude of each peak. For example in Figure 2c, the temperature amplitude peak is 15 K at z ∼50 km and λ_z ∼20 km, and with our quadratic fit the "true peak" is 19 K. The total temperature amplitude and total momentum flux for each profile pair at each altitude are computed as the sum over all detected peaks. Each peak corresponds to a particular vertical wavelength and zonal wavenumber. We compute an average vertical wavelength and zonal wavenumber for each profile pair at each altitude by a weighted average, where the vertical wavelength and zonal wavenumber are weighted with the corresponding temperature amplitude of each peak detected.

In addition to the zonal momentum flux, we estimate the zonal mean drag on the mean flow with

$$F = -\frac{1}{\bar{\rho}} \frac{\delta M_{i,i+1}}{\delta z} \tag{6}$$

and call this the "potential drag" because it is non-directional, and in reality there is an undetermined amount of cancellation between eastward and westward (positive and negative) flux and drag. The uncertainties of this method are discussed in more detail in Ern et al. (2011) and Alexander and Ortland (2010).

The minimum observable horizontal wavelength is twice the separation distance between profiles and shorter wavelengths may be aliased to longer values (e.g., Ern et al., 2004; Eckermann & Preusse, 1999). Since zonal wavenumber is in the numerator of Equation 5, our momentum fluxes most likely have a low-bias. As stated previously we assume that the separation between adjacent profiles near the turnaround latitude is zonal in orientation, so the wavelengths we observe and the momentum fluxes we compute are assumed to be the zonal components thereof. The zonal component is most important to the momentum budget at these latitudes.

3 Gravity wave properties

In this section we present GW properties derived from the S-Transform method discussed in the previous section. These GW properties include temperature amplitude, momentum flux, horizontal wavenumber, and vertical wavelength. Our GW analysis was performed on all adjacent profile pairs between 61° and 63.4°S from May to November for each year of HIRDLS data. Figure 3 shows HIRDLS temperature perturbation amplitudes for the winter and spring seasons for each year. The data is binned 5° in longitude and 2.4° in latitude (61°–63.4°S) and averaged between 35 and 45 km altitude. The top panels are averaged over the winter months of June, July, and August. The bottom panels are averaged over the spring months of September, October, and November.

The winter season shows peaks over the peninsula, although there is considerable wave activity over large non-orographic areas. During the spring months temperature amplitude peaks are smaller but have a similar spatial pattern. The most apparent consistency among each year and seasonal average is the geographic location of the hot spot over the Peninsula. This GW hot spot is an important feature in the Southern Hemisphere, which we will explore in more detail in the following sections.

Figure 4 shows HIRDLS average GW properties for the month of September 2006, in 5° longitude bins and averaged from 61° to 63.4°S. Temperature perturbation amplitude, $|\hat{T}|$ (top left), momentum flux, M (top right), zonal wavenumber, k (bottom left), and vertical wavelength, λ_z (bottom right) are shown as a function of longitude and altitude. These averages only include nonzero momentum fluxes. That is, where the momentum flux is zero, we do not include the corresponding temperature perturbation amplitude, momentum flux, zonal wavenumber, and vertical wavelength in the means. Note that we have the most confidence in the results in the middle of the altitude range displayed in Figure 4, and the results in the lower and upper portions of

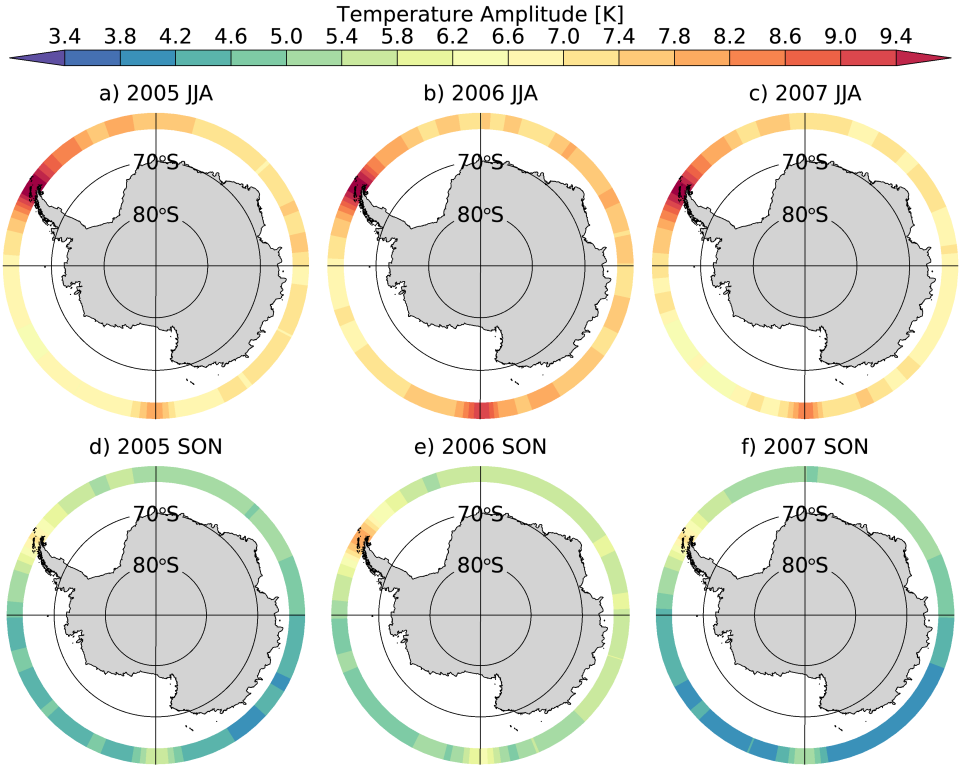

Figure 3. Polar view of Antarctica with HIRDLS temperature perturbation amplitudes averaged between 35 and 45 km altitudes. Top three panels are averaged over June, July, and August for each year. Bottom three panels are averaged over September, October, and November for each year.

the domain are to be used with caution because they may suffer from contamination from the zero-padding effects of the S-transform. The panel on the right shows the MERRA-2 mean wind profile averaged for the month of September.

In general, the largest temperature perturbation amplitudes are between 40 and 70°W, above the Antarctic Peninsula and increase with increasing altitude. The peak in temperature perturbation amplitude corresponds to large momentum fluxes that decrease with increasing altitude, with a sharp decrease in momentum flux where zonal wind peaks near 40 km. The absolute momentum flux values are reasonable for this region compared to other studies using satellite observations to estimate momentum flux (e.g., Ern et al., 2004; Alexander et al., 2008; Geller et al., 2013; Hindley et al., 2020). These studies also show localized spots of enhanced temperature amplitude and momentum flux over the Andes, just north of the Antarctic Peninsula.

The area of large temperature perturbation amplitudes and momentum fluxes also corresponds to smaller horizontal scales (larger k) and slightly longer vertical wavelengths. Vertical wavelengths range between approximately 10 to 17 km and decrease with altitude, especially where winds are increasing. Refraction of GWs can occur when either the buoyancy frequency or intrinsic phase speed changes with altitude as elucidated by the dispersion relation for medium frequency GWs, $|m| = N/|\hat{c_h}|$, where m is the vertical wavenumber, N is the buoyancy frequency, and $\hat{c_h} = c - u$ is the horizontal intrinsic phase speed. The intrinsic phase speed is the phase speed that would be observed in a frame of reference moving with the background

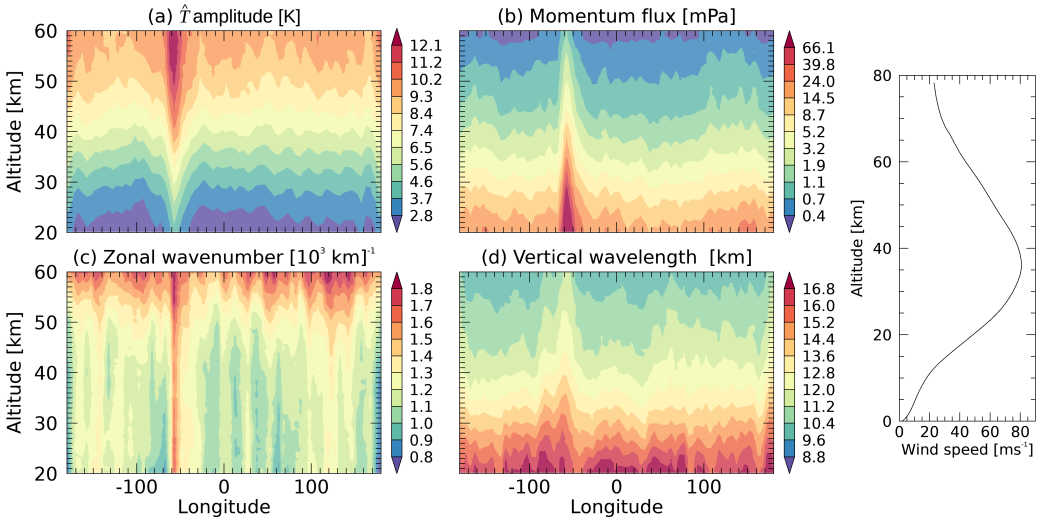

Figure 4. Monthly mean (a) temperature perturbation ($\hat{T}$) amplitude, (b) GW absolute momentum flux, (c) zonal wavenumber, and (d) vertical wavelength as a function of longitude and height for September 2006. The panel on the right is the MERRA-2 zonal wind profile averaged for the month of September 2006 and 61° to 63.4°S.

wind. The decrease in λ_z with altitude is certainly partly due to the increase in N in the stratosphere with altitude.

The relationship to the zonal wind is less straightforward, but Figure 4 shows that the winds increase with height up ∼40 km then decrease. The dispersion relation therefore dictates that the intrinsic phase speed of westward propagating waves would increase below ∼40 km and decrease above, corresponding to decreasing m (increasing λ_z) below ∼40 km and increasing m (decreasing λ_z) above ∼40 km. Likewise the intrinsic phase speed of eastward propagating waves would decrease below ∼40 km and increase above, corresponding to increasing m (decreasing λ_z) below ∼40 km and decreasing m (increasing λ_z) above ∼40 km. Additionally, as will be shown in Section 3.2, GWs with larger momentum fluxes are associated longer vertical wavelengths at 20 km (see Figure 7), and those GWs with larger momentum fluxes break lower in altitude. To summarize, the decrease of λ_z below ∼40 km in Figure 4 is probably due to a combination of eastward propagating GWs refracting to shorter λ_z as they approach critical levels, increasing N, and breaking of GWs with larger momentum fluxes and longer λ_z.

3.1 Zonal mean momentum flux and relationship to zonal mean zonal wind

Figure 5 shows HIRDLS zonal mean momentum fluxes as a function of time and altitude from May through November for each year of HIRDLS data. The black contours show winds from MERRA-2 with 10 ms^{-1} intervals and the solid dark line is the zero-wind line. The overall shape of the momentum flux roughly corresponds to the winds (i.e., momentum flux decreases as zonal mean zonal wind increases), particularly when the zero-wind line descends in late September to mid October when the momentum flux drops off sharply. However, individual peaks in the momentum flux do not appear to correspond to individual peaks in the stratospheric winds in either the nonorographic or orographic region. We point out that although it looks as though the momentum flux over the orographic region is more intermittent than

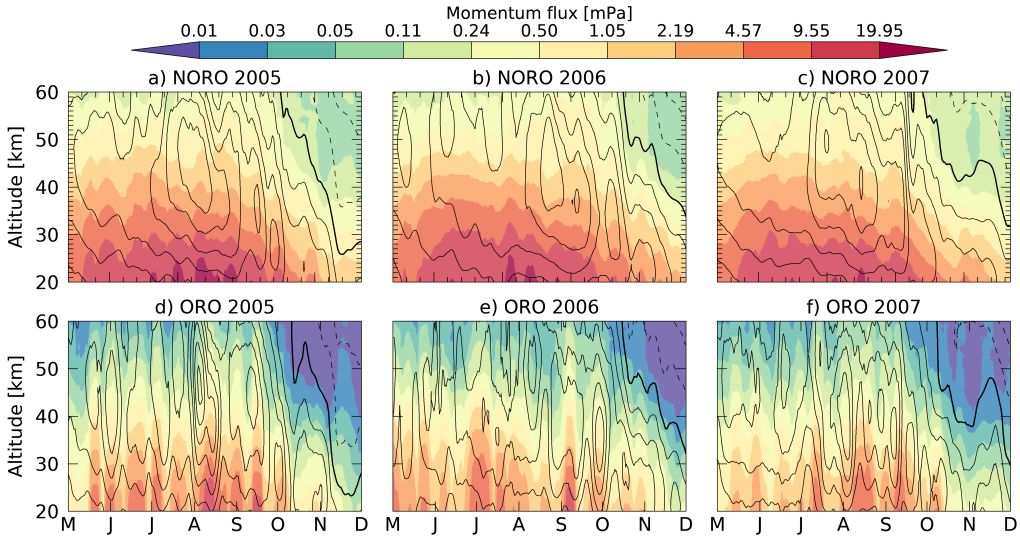

Figure 5. Zonal mean GW momentum flux for nonorographic (a-c) and orographic (d-f) regions from May to November for 2005-2007 averaged from 61°S and 63.4°S. The zonal mean zonal wind from MERRA-2 is shown in the black contours with contour intervals of 10 ms^{-1}. Eastward and westward winds are shown with solid and dashed lines, respectively and the zero wind line is indicated by the thick contour line. The momentum flux is smoothed with a 7-day boxcar average.

over the nonorographic region, this is because the nonorographic region is so much larger than the orographic region (330° versus 30° longitude) that there are many more profiles in the nonorographic region and this results in a smoother appearance. A 30° subsample over the nonorographic region shows just as much intermittency (not shown).

Next we investigate the relationship between zonal wind at different altitudes and GW absolute momentum flux in the middle of our altitude range, where we have the most confidence in our results. Figure 6 shows HIRDLS absolute momentum fluxes averaged between 35 and 45 km and between 40° and 70°W (black, left axis) and MERRA-2 near-surface winds averaged between 1 and 3 km and between 40° and 70°W and 63°S and 66°S (gray, right axis) for the three years of HIRDLS data. Again, we are calling the region between 40 and 70°W orographic because this is the only region with orographic features between 61°S and 63.4°S. We chose 63°S and 66°S for the MERRA-2 near-surface winds because this is directly over the Antarctic Peninsula. Both the momentum flux and the wind are smoothed with a 3-day boxcar average. The linear Pearson correlation coefficient, r, of the two time series between May and the end of September is also shown in the corresponding panel. The GW absolute momentum flux is highly correlated with the near-surface winds, especially in 2005 and 2006, between May and September. The sudden decrease of momentum flux to near zero in October in all three years is due to the descent of the zero wind line near 40 km. The year with the strongest correlation, 2006, also has the strongest near-surface westerlies. The winds in the chosen region rarely drop below 0 ms^{-1} between May and September. The near-surface winds in 2005 also rarely drop below 0 ms^{-1} between May and September, but the magnitude of the winds isn't as large as in 2006. However, in 2007, the year with the lowest correlation coefficient, the winds

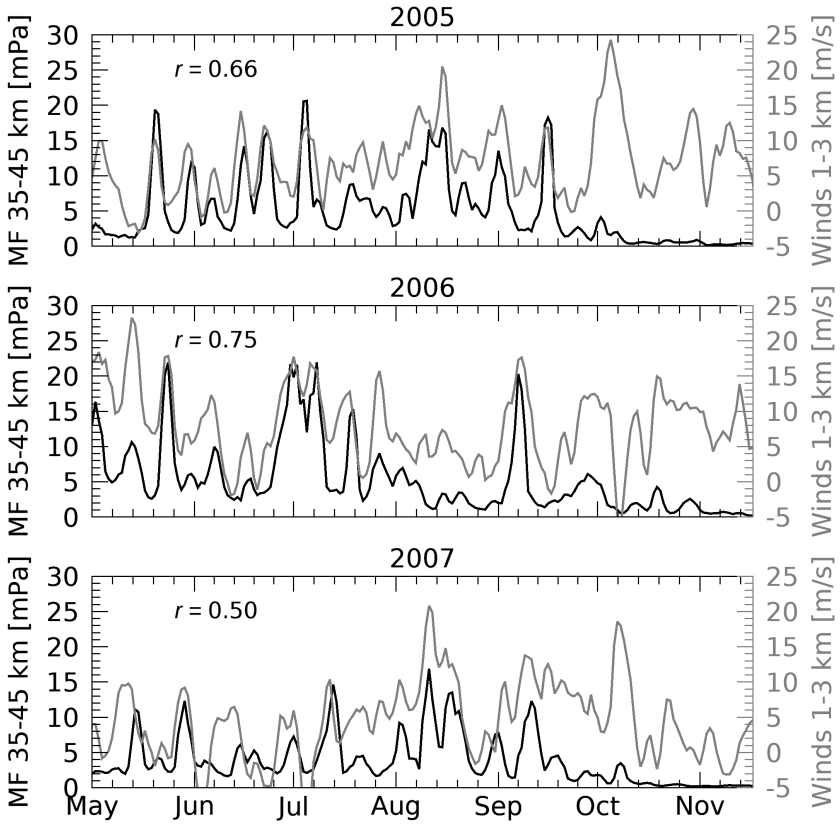

Figure 6. HIRDLS momentum fluxes averaged between 35 and 45 km and between 40° and 70°W (black, left axis) and MERRA-2 near-surface winds averaged between 1 and 3 km (gray, right axis) for the three years of HIRDLS data. The linear Pearson correlation coefficient, r, of the two time series in each plot is also shown in the corresponding panel.

frequently drop below 0 ms^{-1} and the maximum peaks rarely exceed 10 ms^{-1} before August.

We also performed this analysis for winds at different altitudes, and the relationship between winds at higher levels and GW absolute momentum flux isn't as strong. For example, the correlation coefficients of the winds between 10 and 25 km and 60°S and 64°S and the fluxes is 0.47, 0.44, and 0.24 for 2005, 2006, and 2007, respectively and the correlation coefficients of the winds between 27 and 35 km and the fluxes is 0.36, 0.09, 0.13 for 2005, 2006, and 2007, respectively. We additionally performed this analysis for all nonorographic longitude bins and found no significant correlations. Altogether, this analysis suggests that the surface winds are the most important factor driving the variability of orographic GW momentum flux in the middle stratosphere and that the strongest westerly surface winds lead to the largest momentum fluxes.

3.2 Statistical properties of GW events

In the previous section we presented results for averages of many wave events: seasonal means, monthly means, and zonal means or zonally averaged properties of wave events. In this section we present the statistical analysis of individual wave events. Figure 7a shows the probability of occurrence of HIRDLS orographic and nonorographic GW absolute zonal momentum fluxes. The distributions are popu-

lated with events from each peak in the covariance spectrum at 20 km from every profile pair between 61° and 63.4°S and from May to Nov 2006. We have not applied any spatial or temporal averaging to the fluxes. The shape of the distributions is approximately lognormal: the dashed lines in (a) show the theoretical lognormal distributions with the same geometric mean and standard deviation as the HIRDLS orographic (black) and nonorographic (gray) momentum fluxes. Many previous studies using both observations and models have shown that GW momentum fluxes have an approximately lognormal distribution with a broad tail of rare but large momentum flux events (e.g., Hertzog et al., 2012; Alexander & Grimsdell, 2013; Wright et al., 2013; de la Cámara et al., 2014; Jewtoukoff et al., 2015; Holt et al., 2017). The contribution of the large events to the total flux can be assessed by computing the percentage of the total flux coming from fluxes larger than a given quantile (Hertzog et al., 2012). The 90th and 99th percentiles are shown in (a) along with the percentage of the total flux coming from fluxes larger than the 90th and 99th percentiles. For both orographic and nonorographic GW events, a considerable portion (67% for orographic and 53% nonorographic) of the total flux is due to the largest 10 percent of events. For orographic events, almost a third of the total momentum flux is due to only 1% of all events. This underlines that these large GW momentum fluxes, while rare, are extremely important for the zonal mean momentum budget.

The black line in Figure 7b shows the probability of occurrence of vertical wavelength for all events shown in (a), orographic and nonorographic combined. Additionally, the blue line is the contribution of the smallest 10% of events and the red line is the contribution of the largest 10% of events. The overall distribution shows an almost uniform distribution between 10 and 40 km. Recall that we excluded vertical wavelengths smaller than the Nyquist wavelength for HIRDLS (2 km) and larger than 40 km. The smallest 10% of fluxes also reflect this lack of preference for vertical wavelength. However, the largest 10% of fluxes are skewed toward longer vertical wavelengths. To evaluate the effects of noise on the results, we performed our analysis on the same HIRDLS profiles replaced with random temperature perturbations with standard deviation of 0.5 K. The gray line shows the distribution for the random noise profiles. The dotted lines, with colors corresponding to the colors of the distributions with solid lines, show the results when no amplitude cutoff is applied to our analysis (i.e., no noise is removed). The results show that without the amplitude cutoff applied to the analysis of the HIRDLS data, the distributions for the total events and the smallest 10% of events start to take on characteristics of the noise distribution: a preference for small vertical wavelengths. The distribution for the largest 10% of events is basically the same whether an amplitude cutoff is included or not. This analysis along with the fact that the noise distribution is a very different shape than the distributions with the amplitude cutoff gives us confidence that our results are due to robust wave events detected by HIRDLS and that our amplitude cutoff is indeed necessary to remove the effects of noise.

The black line in Figure 7c shows the probability of occurrence of zonal wavenumber for all events in (a). Again the blue line is the contribution of the smallest 10% of events, the red line is the contribution of the largest 10% of events, the gray line shows the result for noise, and the dotted lines show the results when no amplitude cutoff is applied to our analysis. The total distribution for zonal wavenumber (black solid line) shows a preference for smaller zonal wavenumbers (larger zonal wavelengths). The zonal wavenumbers corresponding to the smallest 10% of fluxes (blue solid line) are strongly skewed toward smaller wavenumbers. The zonal wavenumbers corresponding to the largest 10% of fluxes (red solid line) are also skewed towards smaller wavenumbers for wavenumbers below about 4 $(1000\ \mathrm{km})^{-1}$, but are much more broadly distributed in general and are almost uniformly distributed for larger zonal wavenumbers. The largest zonal wavenumber is $\sim$7.2 $(1000\ \mathrm{km})^{-1}$, which corresponds to $\sim$139 km zonal wavelength. This is 2 times the shortest zonal distance between HIRDLS

profiles, or the Nyquist cutoff. HIRDLS may be sensitive to waves with zonal wavelengths as short as about 10 km, but these waves are undersampled (Alexander et al., 2008). Waves with wavelengths below the Nyquist cutoff will be aliased into longer wavelengths (smaller wavenumbers). There is another bump in the zonal wavenumber distribution at $\sim$3.6 (1000 km)$^{-1}$ (278 km zonal wavelength). This is because the HIRDLS profiles are in pairs: the zonal distance of the pairs is $\sim$69 km and is $\sim$139 km from one pair to the next for this measurement period (see Figure 1). The bump at $\sim$3.6 (1000 km)$^{-1}$ is due to aliasing of zonal wavelengths longer than $\sim$139 km.

For a set of zonal waves smaller than the Nyquist cutoff, the distribution of zonal wavenumbers is expected be uniform. This is because the phase difference, $\Delta\phi_{i,i+1}$, is random and uniformly distributed (Ern et al., 2004). Similarly, if adjacent profiles have perturbations from different waves (or random fluctuations from noise), phase differences will also be random and uniformly distributed. This is apparent in the wavenumber distribution for noise (gray line, 7c). The distribution of zonal wavenumber with no amplitude cutoff applied (black dotted line) is quite uniform in distribution. Some of this uniformity is removed when the amplitude cutoff is applied (solid black line), especially at the smaller zonal wavenumbers. However, some uniformity is still apparent as zonal wavenumber grows. This uniformity is most likely due to the aliasing of waves below the Nyquist cutoff instead of noise. This is more apparent in the distribution for the highest 10% of momentum fluxes (red solid line), which is quite uniform. Furthermore, the distribution for the highest 10% of momentum fluxes is virtually unchanged when the amplitude cutoff is applied, suggesting that the uniformity in this distribution is indeed due to aliasing of waves below the Nyquist cutoff. On the other hand, the zonal wavenumber distribution for the lowest 10% of momentum fluxes shows a very strong preference for small wavenumbers with no hints of uniformity in the distribution. It is also drastically impacted by including the amplitude cutoff (difference between blue dotted and solid lines). All of this suggests that the momentum flux estimates for the smallest fluxes are more accurate than for the largest fluxes, and that the largest fluxes are underestimated (since zonal wavenumber, k is in the numerator of Equation (5)).

4 Gravity Wave Potential Zonal Drag

In this section we present estimates of the zonal mean zonal GW drag estimated by HIRDLS. We estimate this quantity with the vertical derivative of absolute momentum flux, as shown in Equation 6. We call this the "potential drag" because it is non-directional, and there is an undetermined amount of cancellation between eastward and westward (positive and negative) GW drag. The uncertainties of this method are discussed in more detail in Ern et al. (2011) and Alexander and Ortland (2010). Although the drag we calculate is not a vector quantity, we can use the direction of the wind and the dispersion relation to interpret the direction of the force on the zonal mean flow. For example, the momentum fluxes above mountains are typically assumed to be from GWs propagating westward against the zonal mean flow.

Figure 8 shows HIRDLS GW potential drag as a function of longitude and height, averaged from May through November and 61°S and 63.4°S. Again, we emphasize that the results are most reliable between 30-50 km. The peak potential drag occurs over the Antarctic Peninsula and corresponds to the momentum flux peak in Figure 4, but there is considerable variability in the strength of the peak. Although the peak locally over the orographic region is around 4-5 times larger than over the nonorographic regions, the contribution to the zonal mean is greater from nonorographic regions than orographic regions because the area over nonorographic regions is so much larger. This is apparent in Figure 9 which shows the zonal mean GW potential drag as a function of time and altitude averaged between 61°S and 63.4°S for nonorographic (a-c) and

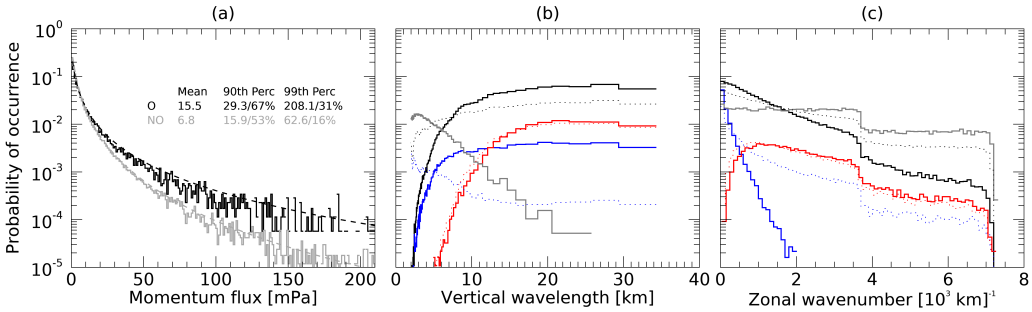

Figure 7. (a) Probability of occurrence of HIRDLS orographic and nonorographic GW absolute momentum fluxes. In (a) the mean momentum flux and 90th and 99th percentiles of the distributions are displayed (in mPa) along with the percentage of the total flux corresponding to fluxes larger than the 90th and 99th percentiles. (b) The black line shows the probability of occurrence of vertical wavelength for all events shown in (a). The blue line is the contribution of the smallest 10% of events and the red line is the contribution of the largest 10% of events. The gray line shows the result for noise (see text). (c) The black line shows the probability of occurrence of zonal wavenumber for all events in (a). Again the blue line is the contribution of the smallest 10 percent of events and the red line is the contribution of the largest 10 percent of events. The gray line shows the result for noise (see text). The dotted lines in (b) and (c) show the results when no amplitude cutoff is applied to our algorithm (i.e., no noise is removed). All quantities in these plots are at 20 km for May–Nov 2006.

orographic (d-f) regions. Again, note that we define the orographic region to be between 40° and 70° W.

The shape of the potential drag in Figure 9 roughly follows the shape of the zonal mean zonal winds (which is more apparent in a-c), i.e., drag increases as zonal mean zonal winds increase. However the short-term variability in the potential drag does not appear to correspond to the short-term variability in the winds in the stratosphere. Recall that Figure 6 showed that the short-term variability of the momentum flux at least over the orographic region is highly correlated with the surface winds. As in Figure 5 we point out that although it looks as though the potential drag over the orographic region is more intermittent than over the nonorographic region, this is because the nonorographic region is so much larger than the orographic region (330° versus 30°) that there are many more profiles in the nonorographic region and this results in a smoother appearance. A 30° subsample over the nonorographic region shows just as much intermittency (not shown).

4.1 HIRDLS GW potential drag and CCMI-1 zonal wave forcing

Figure 10 shows the zonal acceleration due to parameterized GW drag for 9 of the models participating in the Chemistry-Climate Model Initiative (CCMI-1) (Eyring et al., 2013; Hegglin et al., 2015). We included the CCMI-1 models that had zonal acceleration due to paramaterized orographic and nonorographic GWs available in the refC1 zonal mean files. While there are large differences in the magnitude of the zonal GW drag, there is one conspicuous feature that is consistent in all the models: a gap in the zonal forcing near 60°S. This is a result of the way that GW parameterizations are designed. In general, parameterized orographic GWs exert their influence on the upper troposphere and lower stratosphere, whereas parameterized nonorographic gravity waves are important only in the mesosphere (McLandress et al., 2013). This

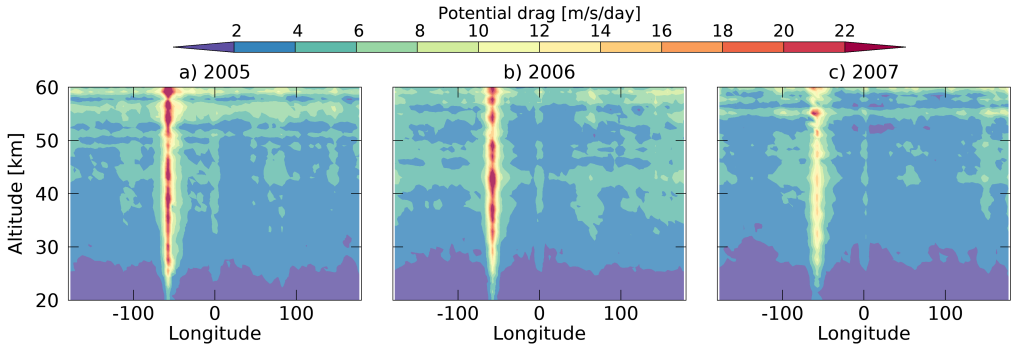

Figure 8. GW potential drag as a function of longitude and height, averaged from May through November for each year and 61°S and 63.4°S.

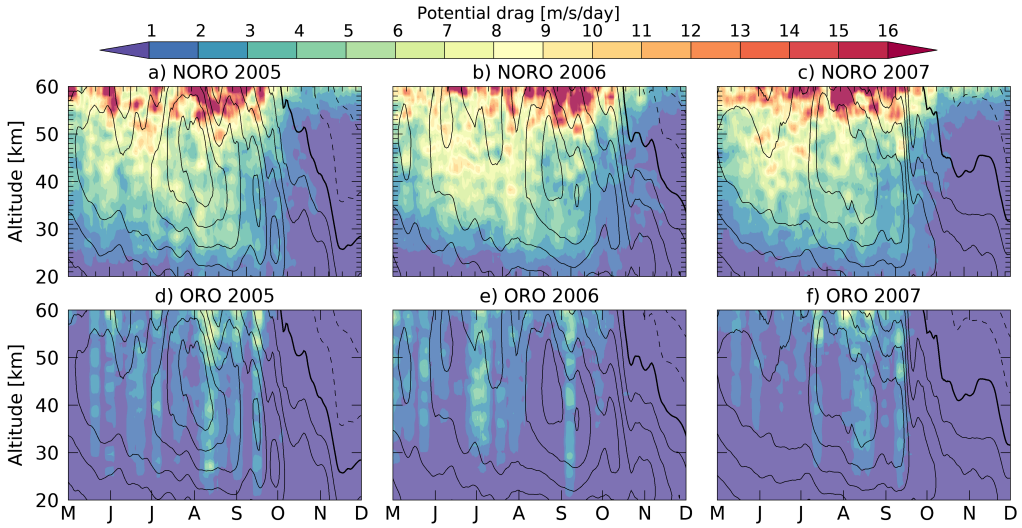

Figure 9. Zonal mean GW potential drag for nonorographic (a-c) and orographic (d-f) regions from May to November for 2005-2007 averaged from 61°S and 63.4°S. The zonal mean zonal wind from MERRA-2 is shown in the black contours with contour intervals of 10 ms^{-1}. Eastward and westward winds are shown with solid and dashed lines, respectively and the zero wind line is indicated by the thick contour line. The potential drag is smoothed with a 7-day boxcar average.

separation of the influence of orographic and nonorographic gravity waves is contrived via the choice of launch amplitudes of gravity waves in the parameterization; larger amplitude waves break lower in altitude. Furthermore, GW parameterizations are column-based, so that parameterized GWs only exert their forces in the column above the grid-cell in which they were launched. Since there is a gap in orographic sources near 60°S, there is a gap in the orographic GW forcing in the stratosphere (where the orographic GW parameterizations are designed to exert their influence).

Recent evidence, however, highlights several shortcomings in the current parameterization methods (see summary by Plougonven et al. (2020)). For example, current parameterizations do not account for large-amplitude nonorographic gravity waves that break in the lower stratosphere (e.g., Hertzog et al., 2008; Plougonven et al.,

2013; Wright et al., 2013; Jewtoukoff et al., 2015; Stephan et al., 2016) or lateral propagation of gravity waves generated at other latitudes (e.g., Sato et al., 2009; Yamashita et al., 2010; Sato et al., 2012; Hindley et al., 2015; Ehard et al., 2017; Krisch et al., 2017; Thurairajah et al., 2017; Strube et al., 2021).

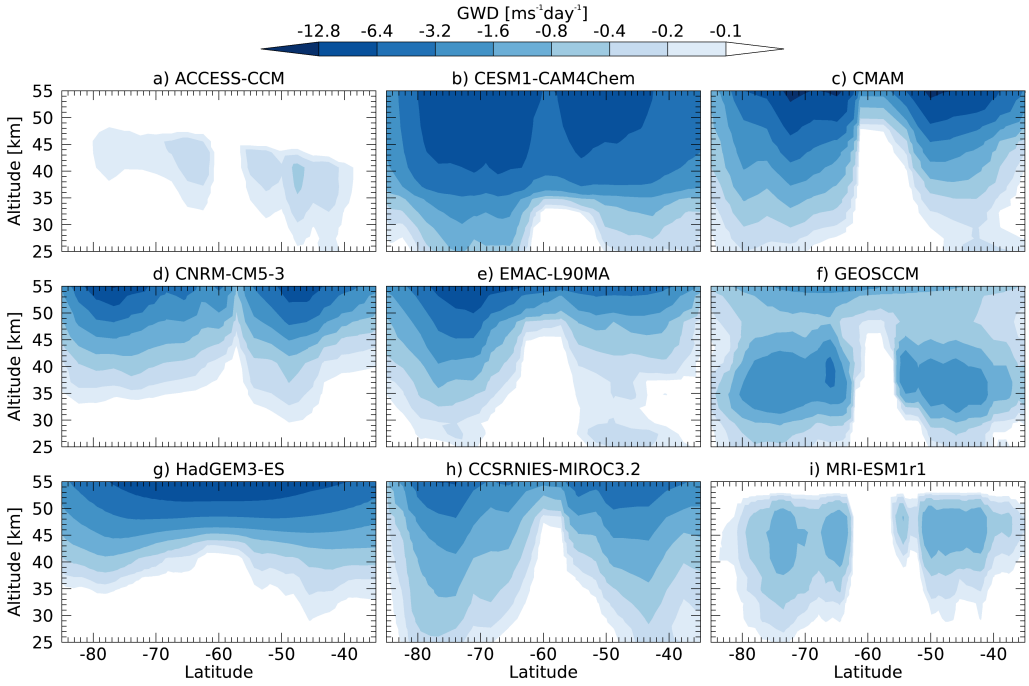

Figure 10. Zonal wind tendency due to parameterized GW drag for 9 of the CCMI-1 models averaged over JJA for 2005-2007.

Figure 11 shows HIRDLS zonal mean potential zonal drag (solid black) compared to zonal EP-flux divergence (blue), and parameterized zonal mean zonal GW drag (red) from the CCMI-1 models averaged between 35 and 45 km. We emphasize that this type of analysis with HIRDLS data is only possible at the narrow latitude band between 61°S and 63.4°S and in this limited height range due to the HIRDLS sampling pattern. For HIRDLS (black line) the contributions to the zonal mean potential zonal drag from waves over nonorographic regions and orographic (between 40° and 70° W) regions are shown with the dashed-dot and dashed line respectively. Although the potential drag is larger locally over orographic regions (see Figure 8), the nonorographic contribution to the zonal mean is larger because the nonorographic region is much larger. HIRDLS potential drag peaks in June or July depending on the year, whereas the CCMI-1 multi-model mean (MMM) resolved EP flux divergence and parameterized GW drag peak in October. Furthermore, the magnitude of the EP flux divergence and parameterized drag in the CCMI-1 MMM is less than the HIRDLS zonal mean potential drag, although the HIRDLS potential drag has large unquantified uncertainties. The HIRDLS results suggest that the CCMI-1 models are missing zonal drag from May through September near 60°S and could explain some of the biases in temperatures and winds and the offset in the timing of the breakdown of the polar vortex in the models. Furthermore, the HIRDLS results suggest that the missing drag near 60°S in Figure 10 is largely over nonorographic regions and support the case made by Hertzog et al. (2008), Plougonven et al. (2013), and Jewtoukoff et al. (2015) that the missing drag near 60°S is from nonorographic sources which, when summed over

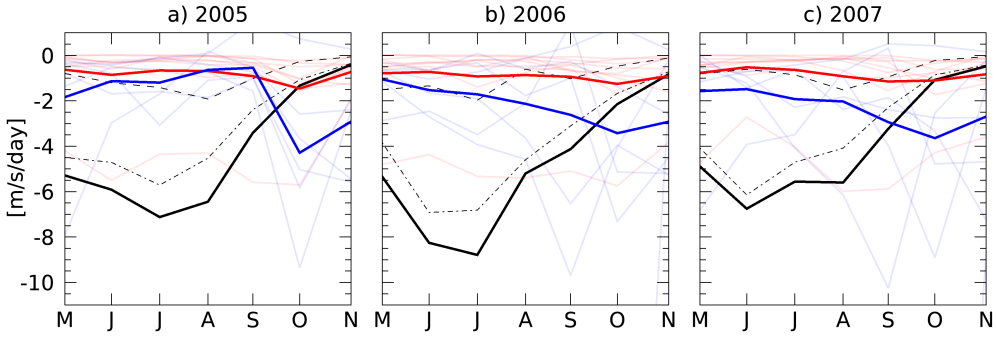

Figure 11. HIRDLS zonal mean potential zonal drag (solid black), CCMI-1 zonal EP flux divergence (blue), and CCMI-1 parameterized zonal mean zonal GW drag (orographic+nonorographic; red) averaged from 35–45 km and between 61°S and 63.4°S for (a) 2005, (b) 2006, and (c) 2007. The contribution to the HIRDLS zonal mean potential zonal drag from nonorographic regions is shown with the dashed-dot line and the contribution from orographic regions with the dashed line. The CCMI-1 multi-model means are shown in thick red and blue and the individual models are shown in the lighter red and blue.

the vast nonorographic areas, eclipse the very localized orographic sources. Because of the study design, these results do not address lateral propagation.

4.2 Discussion of implications for the Brewer-Dobson Circulation and ozone hole

Continuous measurements of ozone concentration and ozone hole size have been recorded since 1979. Within the first decade after the discovery of the ozone hole, Carslaw et al. (1998) found that mountain waves increased stratospheric ozone depletion in the Arctic and suggested that GWs occurring at the vortex edge should be examined for their potential contribution to ozone depletion. The largest ozone hole area in the 41 year record reached a maximum area of ∼29.6 million square kilometers and the polar cap ozone concentration reached a minimum of ∼160 Dobson units in September 2006. This was an extreme peak in ozone hole size that corresponds with large momentum fluxes observed in HIRDLS GWs in September 2006.

Figure 12 shows the zonal mean zonal momentum flux time series for all three consecutive years of HIRDLS data for the total (black), orographic (purple), and nonorographic (blue) GWs. The orographic momentum fluxes are smaller in the zonal mean, while the larger area for the the nonorographic (waves between 40°E and 70°W) gives a larger contribution to the zonal mean. The largest momentum flux occurs in 2006 and corresponds to a large peak in orographic momentum flux. Momentum fluxes in 2006 are higher in general than the other years and the maximum momentum flux for all years of data also occurs in September 2006. Higher gravity wave momentum fluxes near 40 km could indicate deeper GW penetration and less dissipation and drag above the ozone peak. Less drag would also contribute to generally colder temperatures and potentially stronger ozone depletion. Figure 3 showed that average temperature amplitudes were also higher for both orographic and nonorographic GW regions in Sep-Nov 2006 than in the other years. Large gravity wave temperature amplitudes are associated with formation of polar stratospheric clouds (e.g., Dörnbrack et al., 2002; Hoffmann et al., 2017) where heterogeneous chemistry leads to enhanced ozone depletion.

We propose that the edge of the polar vortex and the magnitude of zonal mean momentum flux and temperature amplitudes in our HIRDLS results could be correlated through the symmetry of the ozone hole. The ozone hole/vortex was more symmetric in 2006 and the edge of the vortex coincided with the band near 60°S at most longitudes. The vortex edge is where maximum winds tend to focus wave propagation (Sato et al., 2012) leading to larger momentum fluxes and higher temperature variances in our analysis.

The observations suggest that GWs may be contributing much more to the total zonal forcing than the models suggest. It is also noteworthy that HIRDLS is more likely to observe longer vertical wavelengths in 2006 due to the stronger zonal mean zonal winds at our analysis latitudes. Longer vertical wavelengths suggests that there is greater potential for GWs to propagate higher. In addition, stronger zonal mean zonal winds will be associated with the symmetry of the ozone hole.

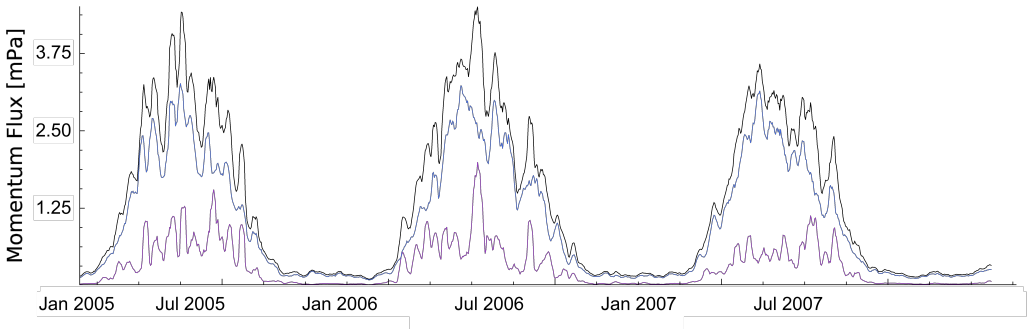

Figure 12. HIRDLS zonal mean zonal momentum flux averaged between 35 and 45 km. The total zonal mean flux is shown in black. Orographic (between 40°W to 70°W) and nonorographic GW contributions to the zonal mean momentum flux are shown in purple and blue, respectively.

5 Summary and Conclusion

In this study, we applied an S-transform analysis to HIRDLS profiles near the turnaround latitude (∼63.4°S) to investigate the missing drag in CCMs in the Southern Hemisphere winter. At the turnaround latitude HIRDLS provides dense zonal sampling, making it an excellent tool for this analysis. While previous studies have used HIRDLS to investigate the largest scale waves between wavenumbers 1 through 8 in the tropics (Alexander et al., 2010) and properties of GWs globally (Alexander et al., 2008; Ern et al., 2011; Wright et al., 2010), this is the first study to focus on the turnaround latitude in the Southern Hemisphere.

In general, HIRDLS observes the largest GW temperature amplitudes and zonal momentum fluxes near the Antarctic Peninsula. The S-transform analysis also shows that orographic GWs have shorter horizontal wavelengths and slighly longer vertical wavelengths than nonorographic GWs. While fluxes are much larger locally over this orographic region, the contribution to the zonal mean flux is roughly 3 times smaller than the contribution over nonorographic regions simply because the nonorographic region is so large. The zonal mean zonal momentum flux has a distinct seasonal pattern, peaking in JJA, and is related to the overall shape of the zonal mean zonal wind. However, short-term variability in the zonal mean zonal momentum flux does not correspond to short-term variability in stratospheric zonal mean zonal wind. Instead, we found that the zonal mean zonal momentum flux is highly correlated with the near surface winds over orographic regions.

As shown in many previous studies, the distribution of GW momentum flux is approximately lognormal. We showed that this is also true near the HIRDLS turnaround latitude and that a considerable portion (67% over the orographic region and 53% over nonorographic region) of the total momentum flux near the turnaround latitude is due to the largest 10% of events. We also found evidence that the tails of the momentum flux distributions are actually much longer: the zonal wavenumber distributions suggest that a considerable amount of aliasing is occurring for small-scale waves. This leads to an underestimate of the momentum flux.

We also provided estimates of the zonal drag and used these estimates to evaluate the parameterized GW drag and resolved wave forcing in models participating in phase 1 of CCMI-1. The HIRDLS zonal drag estimates suggest that the CCMI-1 models have insufficient zonal drag, especially in JJA, and that the majority of the missing drag is over nonorographic regions. Again we found that although the potential drag is larger locally over orographic regions, the nonorographic contribution to the zonal mean is larger because the nonorographic region is much larger. The HIRDLS results suggest that the CCMI-1 models are missing zonal drag from May through September near 60°S and could explain some of the biases in temperatures and winds and the offset in the timing of the breakdown of the polar vortex in the models. Furthermore, the HIRDLS results suggest that the missing drag near 60°S in Figure 10 is largely over nonorographic regions and support the case that the missing drag near 60°S is from nonorographic sources.

There are several important limitations of this study to keep in mind. Because of the study design these results do not address lateral propagation, which has been shown to be significant in many studies. There are also large uncertainties associated with the estimates of both momentum flux and potential drag. It is very difficult to quantify these uncertainties. A major uncertainty in the estimate of potential drag is the unknown cancellation between eastward and westward propagating waves. Consideration of HIRDLS vertical wavelengths and the MERRA-2 zonal mean zonal wind profile makes a compelling argument for both eastward and westward nonorographic wave dissipation below and above the jet maximum. In theory if all of the waves were sufficiently sampled horizontally, it would be possible to determine the propagation direction of the waves through the horizontal phase difference computed with the S-transform. However, because many of the waves are undersampled, the horizontal phase difference for those waves is random and the propagation direction cannot be determined. However, even with these large uncertainties, the HIRDLS results still provide compelling evidence that CCMs should include more nonorographic GW drag near 60°S.

Acknowledgments

This work was supported by the NASA New (Early Career) Investigator Program (NIP) in Earth Science (NASA Grant No. 80NSSC18K0768), as well as the NASA Aura Science Team (NASA Grant No. 80NSSC18K0069 and NASA Grant No. 80NSSC20K0950). HIRDLS data was obtained from Goddard Earth Sciences (GES) Data and Information Services Center (DISC) `https://disc.gsfc.nasa.gov/datasets/HIRDLS2_007/summary`. MERRA-2 data was also obtained from NASA GES DISC (`doi:10.5067/QBZ6MG944HW0`). The CCMI-1 data was obtained on 4 January 2022 from `http://catalogue.ceda.ac.uk/uuid/9cc6b94df0f4469d8066d69b5df879d5` except for the CESM1 data, which was obtained via `https://tds.ucar.edu/thredds/catalog/esgcet/133/ccmi1.output.NSF-DOE-NCAR.CESM1-CAM4Chem.refC1.mon.atmos.r1i1p1.v20170825.xml`. We acknowledge the modeling groups for making their simulations available for this analysis, the joint WCRP SPARC/IGAC Chemistry-Climate Model Initiative (CCMI) for organizing and coordinating the model data analysis activity,

and the British Atmospheric Data Centre (BADC) for collecting and archiving the CCMI model output.

References

Alexander, M. J., & Barnett, C. (2007). Using satellite observations to constrain parameterizations of gravity wave effects for global models. *J. Atmos. Sci.*, *64*, 1652–1665. doi: 10.1175/JAS3897.1

Alexander, M. J., Eckermann, S. D., Broutman, D., & Ma, J. (2009). Momentum flux estimates for South Georgia Island mountain waves in the stratosphere observed via satellite. *Geophys. Res. Lett.*, *36*. doi: 10.1029/2009GL038587

Alexander, M. J., Geller, M., McLandress, C., Polavarapu, S., Preusse, P., Sassi, F., ... Watanabe, S. (2010). Recent developments in gravity wave effects in climate models, and the global distribution of gravity wave momentum flux from observations and models. *Q. J. Royal Meteorological Society*, *136*, 1103-1124. doi: doi:10.1002/qj.637

Alexander, M. J., Gille, J., Cavanaugh, C., Coffey, M., Craig, C., Eden, T., ... Dean, V. (2008). Global estimates of gravity wave momentum flux from High Resolution Dynamics Limb Sounder observations. *Journal of Geophysical Research*, *113*(D15), D15S18. doi: 10.1029/2007JD008807

Alexander, M. J., & Grimsdell, A. W. (2013). Seasonal cycle of orographic gravity wave occurrence above small islands in the southern hemisphere: Implications for effects on the general circulation: Gravity waves above sh islands. *Journal of Geophysical Research: Atmospheres*, *118*(20), 11,589-11,599. doi: 10.1002/2013JD020526

Alexander, M. J., & Ortland, D. A. (2010). Equatorial waves in high resolution dynamics limb sounder (hirdls) data. *J. Geophys. Res.*, *115*(D24111). doi: doi:10.1029/2010JD014782

Arblaster, J. M., Gillett (Lead authors), N. P., Calvo, N., Forster, P. M., Polvani, L. M., Son, S.-W., ... Young, P. J. (2014). *Stratospheric Ozone Changes and Climate, Chapter 4 in. Scientific Assessment of Ozone Depletion: 2014*, Global Ozone Research and Monitoring Project-Report No. 55, World Meteorological Organization, Geneva, Switzerland.

Butchart, N., Charlton-Perez, A. J., Cionni, I., Hardiman, S. C., Haynes, P. H., Krüger, K., ... Yamashita, Y. (2011). Multimodel climate and variability of the stratosphere. *Journal of Geophysical Research*, *116*(D5), D05102. doi: 10.1029/2010JD014995

Carslaw, K. S., Wirth, M., Tsias, A., Luo, B. P., Dornbrack, A., Leutbecher, M., ... Peter, T. (1998). Increased stratospheric ozone depletion due to mountain-induced atmospheric waves. *Letters to Nature*, *391*, 675-678.

de la Cámara, A., & Lott, F. (2015). A parameterization of gravity waves emitted by fronts and jets. *Geophys. Res. Lett.*, *42*, 2071–2078. doi: 10.1002/2015GL063298

de la Cámara, A., Lott, F., & Hertzog, A. (2014). Intermittency in a stochastic parameterization of nonorographic gravity waves. *Journal of Geophysical Research: Atmospheres*, *119*(21), 11,905-11,919. doi: 10.1002/2014JD022002

de la Cámara, A., Lott, F., Jewtoukoff, V., Plougonven, R., & Hertzog, A. (2016). On the gravity wave forcing during the Southern Hemisphere final warming in LMDZ. *J. Atmos. Sci.*, *73*, 3213–3226. doi: 10.1175/JAS-D-15-0377.1

Dörnbrack, A., Birner, T., Fix, A., Flentje, H., Meister, A., Schmid, H., ... Mahoney, M. J. (2002). Evidence for inertia gravity waves forming polar stratospheric clouds over scandinavia. *Journal of Geophysical Research Atmospheres*, *107*(D20), SOL 30-1-SOL 30-18. doi: https://doi.org/10.1029/2001JD000452

Eckermann, S. D., & Preusse, P. (1999). Global measurements of stratospheric mountain waves from space. *Science*, *286*, 1534–1537. doi: 10.1126/science.286

.5444.1534

Ehard, B., Kaifler, B., Dornbrack, A., Preusse, P., Eckermann, S., Bramberger, ... Rapp, M. (2017). Horizontal propagation of large-amplitude mountain waves into the polar night jet. *J. Geophys. Res. Atmos.*, *122*, 1423–1436.

Ern, M., Preusse, P., Alexander, M. J., & Warner, C. (2004). Absolute values of gravity wave momentum flux derived from satellite data. *Journal of Geophysical Research*, *109*(D20), D20103. doi: 10.1029/2004JD004752

Ern, M., Preusse, P., Gille, J. C., Hepplewhite, C. L., Mlynczak, M. G., Russell III, J. M., & Riese, M. (2011). Implications for atmospheric dynamics derived from global observations of gravity wave momentum flux in stratosphere and mesosphere. *JOURNAL OF GEOPHYSICAL RESEARCH*, *116*(D19107). doi: 10.1029/2011JD015821

Eyring, V., Lamarque, J.-F., Hess, P., Arfeuille, F., Bowman, K., Chipperfiel, M. P., ... Young, P. J. (2013). Overview of IGAC/SPARC Chemistry-Climate Model Initiative (CCMI) community simulations in support of upcoming ozone and climate assessments. *SPARC Newsletter*, *40*, 48–66.

Eyring, V., Shepherd, T. G., & Waugh—Eds., D. W. (2010). *SPARC CCMVal report on the evaluation of chemistry-climate models.* SPARC Rep. 5, WCRP-132, WMO/TD-No. 1526, available online: http://www.sparc-climate.org/publications/sparc-reports/sparc-report-no5.

Garcia, R. R., Smith, A. K., Kinnison, D. E., Cámara, A. d. l., & Murphy, D. J. (2017). Modification of the gravity wave parameterization in the whole atmosphere community climate model: Motivation and results. *Journal of the Atmospheric Sciences*, *74*(1), 275-291. doi: 10.1175/JAS-D-16-0104.1

Geller, M. A., Alexander, M. J., Love, P. T., Bacmeister, J., Ern, M., Hertzog, A., ... Zhou, T. (2013). A comparison between gravity wave momentum fluxes in observations and climate models. *J. Climate*, *26*, 6383–6405. doi: 10.1175/JCLI-D-12-00545.1

Gille, J., Barnett, J., Arter, P., Barker, M., Bernath, P., Boone, C., ... Young, G. (2008). High resolution dynamics limb sounder: Experiment overview, recovery, and validation of initial temperature data. *Journal of Geophysical Research*, *113*(D16), D16S43. doi: 10.1029/2007JD008824

Hegglin, M., Lamarque, J., & Eyring, V. (2015). *The IGAC/SPARC Chemistry-Climate Model Initiative Phase-1 (CCMI-1) model data output.* NCAS British Atmospheric Data Centre, accessed January 4, 2022. (http://catalogue.ceda.ac.uk/uuid/9cc6b94df0f4469d8066d69b5df879d5)

Hendricks, E. A., Doyle, J. D., Eckermann, S. D., Jiang, Q., & Reinecke, P. A. (2014). What is the source of the stratospheric gravity wave belt in Austral winter? *J. Atmos. Sci.*, *71*, 1583–1592. doi: 10.1175/JAS-D-13-0332.1

Hertzog, A., Alexander, M. J., & Plougonven, R. (2012). On the intermittency of gravity wave momentum flux in the stratosphere. *Journal of the Atmospheric Sciences*, *69*(11), 3433-3448. doi: 10.1175/JAS-D-12-09.1

Hertzog, A., Boccara, G., Vincent, R. A., Vial, F., & Cocquerez, P. (2008). Estimation of gravity wave momentum flux and phase speeds from quasi-Lagrangian stratospheric balloon flights. Part II: Results from the Vorcore campaign in Antarctica. *J. Atmos. Sci.*, *65*, 3056–3070. doi: 10.1175/2008JAS2710.1

Hindley, N. P., Smith, N. D., Wright, C. J., Rees, D. A. S., & Mitchell, N. J. (2016). A two-dimensional stockwell transform for gravity wave analysis of airs measurements. *Atmos. Meas. Tech.*, *9*, 2545–2565. doi: 10.5194/amt-9-2545-2016

Hindley, N. P., Wright, C. J., Hoffmann, L., Moffat-Griffin, T., & Mitchell, N. J. (2020). An 18-year climatology of directional stratospheric gravity wave momentum flux from 3-D satellite observations. *Geo. Res. Lett.*, *47*, e2020GL089557. doi: 10.1029/2020GL089557

Hindley, N. P., Wright, C. J., Smith, N. D., Hoffmann, L., Holt, L. A., Alexander, M. J., ... Mitchell, N. J. (2019). Gravity waves in the winter strato-

sphere over the southern ocean: high-resolution satellite observations and 3-d spectral analysis. *Atmos. Chem. Phys.*, *19*, 15377–15414. doi: 10.5194/acp-19-15377-2019

Hindley, N. P., Wright, C. J., Smith, N. D., & Mitchell, N. J. (2015). The southern stratospheric gravity wave hot spot: individual waves and their momentum fluxes measured by cosmic gps-ro. *Atmos. Chem. Phys.*, *15*, 7797–7818. doi: 10.5194/acp-15-7797-2015

Hoffmann, L., Spang, R., Orr, A., Alexander, M. J., Holt, L. A., & Stein, O. (2017). A decadal satellite record of gravity wave activity in the lower stratosphere to study polar stratospheric cloud formation. *Atmospheric Chemistry and Physics*, *17*(4), 2901–2920. doi: 10.5194/acp-17-2901-2017

Holt, L. A., Alexander, M. J., Coy, L., Liu, C., Molod, A., Putman, W., & Pawson, S. (2017). An evaluation of gravity waves and gravity wave sources in the Southern Hemisphere in a 7 km global climate simulation: Gravity Waves in the Southern Hemisphere. *Quarterly Journal of the Royal Meteorological Society*, *143*(707), 2481–2495. doi: 10.1002/qj.3101

Jewtoukoff, V., Hertzog, A., & Pougonven, R. (2015). Comparison of gravity waves in the Southern Hemisphere derived from balloon observations and the ECMWF analyses. *J. Atmos. Sci.*, *72*, 3449–3468. doi: 10.1175/JAS-D-14-0324.1

Jiang, Q., Doyle, J. D., Reinecke, A., Smith, R. B., & Eckermann, S. D. (2013). A modeling study of stratospheric waves over the Southern Andes and Drake Passage. *J. Atmos. Sci.*, *70*, 1668–1689. doi: 10.1175/JAS-D-12-0180.1

Krisch, I., Preusse, P., Ungermann, J., Dörnbrack, A., Eckermanna, S., Ern, M., ... Riese, M. (2017). First tomographic observations of gravity waves by the infrared limb imager GLORIA. *Atmos. Chem. Phys.*, *17*, 14937–14953.

McLandress, C., Scinocca, J. F., Theodore G. Shepherd, M. C. R., & Manney, G. L. (2013). Dynamical control of the mesosphere by orographic and nonorographic gravity wave drag during the extended Northern Winters of 2006 and 2009. *J. Atmos. Sci.*, *70*, 2152–2169.

McLandress, C., Shepherd, T. G., Polavarapu, S., & Beagley, S. R. (2012). Is missing orographic gravity wave drag near 60°s the cause of the stratospheric zonal wind biases in chemistry–climate models? *Journal of the Atmospheric Sciences*, *69*(3), 802-818. doi: 10.1175/JAS-D-11-0159.1

Plougonven, R., de la Cámara, A., Hertzog, A., & ois Lott, F. (2020). How does knowledge of atmospheric gravity waves guide their parameterizations? *Quart. J. Roy. Meteor. Soc.*, *146*, 1529–1543. doi: 10.1002/qj.3732

Plougonven, R., Hertzog, A., & Guez, L. (2013). Gravity waves over antarctica and the southern ocean: consistent momentum fluxes in mesoscale simulations and stratospheric balloon observations. *Quarterly Journal of the Royal Meteorological Society*, *139*(670), 101-118. doi: 10.1002/qj.1965

Sato, K., Tateno, S., Watanabe, S., & Kawatani, Y. (2012). Gravity Wave Characteristics in the Southern Hemisphere Revealed by a High-Resolution Middle-Atmosphere General Circulation Model. *Journal of the Atmospheric Sciences*, *69*(4), 1378-1396. doi: 10.1175/JAS-D-11-0101.1

Sato, K., Watanabe, S., Kawatani, Y., Tomikawa, Y., Miyazaki, K., & Takahashi, M. (2009). On the origins of mesospheric gravity waves. *Geophys. Res. Lett.*, *36*. doi: 10.1029/2009GL039908

Shibuya, R., Sato, K., Tomikawa, Y., Tsutsumi, M., & Sato, T. (2015). A study of multiple tropopause structures caused by inertia-gravity waves in the Antarctic. *J. Atmos. Sci.*, *72*, 2109–2130. doi: 10.1175/JAS-D-14-0228.1

Stephan, C., Alexander, M. J., & Richter, J. (2016). Characteristics of gravity waves from convection and implications for their parameterization in global circulation models. *J. Atmos. Sci.*, *73*, 2729–2742. doi: 10.1175/JAS-D-15-0303.1

Stockwell, R. G., Mansinha, L., & Lowe, R. (1996, 05). Localization of the complex

spectrum: the s transform. ieee trans signal process 44: 998-1001. *Signal Processing, IEEE Transactions on*, *44*, 998 - 1001. doi: 10.1109/78.492555

Stockwell, R. G., Riggin, D. M., French, W. J. R., Burns, G. B., & Murphy, D. J. (2007). Planetary waves and intraseasonal oscillations at davis, antarctica, from undersampled time series. *Journal of Geophysical Research: Atmospheres*, *112*(D21). Retrieved from `https://agupubs.onlinelibrary.wiley.com/doi/abs/10.1029/2006JD008034` doi: 10.1029/2006JD008034

Strube, C., Preusse, P., Ern, M., & Riese, M. (2021). Propagation paths and source distributions of resolved gravity waves in ECMWF-IFS analysis fields around the southern polar night jet. *Atmos. Chem. Phys.*, *21*, 18641–18668. doi: 10.5194/acp-21-18641-2021

Thurairajah, B., Siskind, D., Bailey, S., Carstens, J., Russell III, J., & Mlynczak, M. (2017). Oblique propagation of monsoon gravity waves during the Northern Hemisphere 2007 summer. *J. Geophys. Res.*, *122*, 5063–5075.

Wright, C. J., & Gille, J. C. (2013). Detecting overlapping gravity waves using the s-transform. *Geophys. Res. Lett.*, *40*, 1850–1855. doi: 10.1002/grl.50378

Wright, C. J., Osprey, S. M., Barnett, J. J., Gray, L. J., & Gille, J. C. (2010). High resolution dynamics limb sounder measurements of gravity wave activity in the 2006 arctic stratosphere. *Journal of Geophysical Research*, *115*(D02105). doi: doi:10.1029/2009JD011858

Wright, C. J., Osprey, S. M., & Gille, J. C. (2013). Global observations of gravity wave intermittency and its impact on the observed momentum flux morphology: Global gw intermittency and morphology. *Journal of Geophysical Research: Atmospheres*, *118*(19), 10,980-10,993. doi: 10.1002/jgrd.50869

Yamashita, C., Liu, H.-L., & Chu, X. (2010). Gravity wave variations during the 2009 stratospheric sudden warming as revealed by ECMWF-T799 and observations. *Geophys. Res. Lett.*, *37*.